

PAPER

Nanocrystalline W-based alloys with ultrahigh hardness and exceptional irradiation tolerance

To cite this article: Z.M. Wu *et al* 2019 *Nucl. Fusion* **59** 106050

View the [article online](#) for updates and enhancements.



IOP | ebooks™

Bringing you innovative digital publishing with leading voices
to create your essential collection of books in STEM research.

Start exploring the collection - download the first chapter of
every title for free.

Nanocrystalline W-based alloys with ultrahigh hardness and exceptional irradiation tolerance

Z.M. Wu^{1,b}, J. Zhang^{2,b}, J. Zhang³, J.C. Huang³, Y. Fan¹, X.H. Yu⁴, Y.B. Zhao¹, J.L. Zhu^{2,5}, C.Q. Jin^{4,a}, P. Wang^{6,a} and E.G. Fu^{1,a}

¹ State Key Laboratory of Nuclear Physics and Technology, School of Physics, Peking University, Beijing 100871, China

² Center for High Pressure Science and Technology Advanced Research (HPSTAR), Beijing 100094, China

³ College of Energy, Xiamen University, Xiamen 361100, China

⁴ Institute of Physics, Chinese Academy of Sciences, Beijing 100190, China

⁵ Department of Physics, Southern University of Science and Technology, Shenzhen 518055, China

⁶ Lanzhou Institute of Chemical Physics, Chinese Academy of Sciences, Lanzhou 730000, China

E-mail: efu@pku.edu.cn, jin@iphy.ac.cn and pengwang@licp.acas.cn

Received 10 March 2019, revised 16 July 2019

Accepted for publication 24 July 2019

Published 9 September 2019



Abstract

Nanocrystalline W-5 wt.% Y_2O_3 (WYO) with an average grain size of 10 nm and W-5 wt.% Y_2O_3 -2.5 wt.% Ni (WYON) with an average grain size of 85 nm were successfully fabricated for the first time using a high-energy ball-milling method followed by a resistance sintering under ultrahigh pressure (RSUHP) technique. Investigation of the microstructure of sintered WYO shows that the intergranular doping of Y_2O_3 grains inhibits the grain growth of W, and investigation of the microstructure of sintered WYON shows that the addition of Ni atoms leads to the grain growth and density increase. The Vickers hardness of sintered WYO and sintered WYON is much higher than that of ITER grade W. The He bubble areal density and swelling of WYO and WYON are much lower than those of ITER grade W, indicating that WYO and WYON possess exceptional higher irradiation tolerance in terms of He ion damage than coarse-grained ITER grade W. This study demonstrates the promising applications of nanocrystallized W-based alloys as plasma-facing materials (PFMs) due to their ultrahigh hardness and excellent radiation tolerance.

Keywords: nanocrystalline tungsten, ultrahigh hardness, grain boundaries, irradiation tolerance, He bubble

Supplementary material for this article is available [online](#)

(Some figures may appear in colour only in the online journal)

1. Introduction

Tungsten (W) is the primary material used for plasma-facing materials (PFMs) in fusion reactors due to its high melting point (3410 °C), low thermal expansion coefficient ($4.5 \mu\text{m K}^{-1}$ at 25 °C), good thermal conductivity (173 W m⁻¹ K⁻¹ at

25 °C), low sputtering yield, low retention of hydrogen and high elevated temperature strength [1–6]. These properties make it possible to use W in the extreme conditions of high temperature, high dose of neutron irradiation and other low-energy particle (D, T and He) irradiation [1, 7–11]. However, there are still restrictions associated with using W as PFMs [12–17], such as low temperature brittleness due to its high ductile-brittle transition temperature (373–673 K), easy

^a Author to whom any correspondence should be addressed.

^b Zaoming Wu and Jun Zhang contributed equally to the work.

growth resulted from low recrystallization temperature (RCT) (1423–1623 K) and serious degradation, e.g. swelling, fracture, bubbles, etc, after long term radiation.

Nanocrystalline materials usually possess excellent mechanical and physical properties, such as higher strength [18–20] and outstanding radiation tolerance [21–23] due to abundant grain boundary regions. Nanocrystalline materials can be considered as two ‘phases’ of grains and grain boundaries (GBs). The refinement of W grains will enhance the strength (such as hardness and yield strength). Furthermore, the GB volume fraction increases sharply as the grain size is smaller than 100 nm, and the GB volume fraction is 50% when the grain size is 5 nm. The GBs act as dislocation sources and dislocation sinks, and this will improve the radiation tolerance. The refinement of grain size could reduce the ductile brittle transition temperature (DBTT) and improve low temperature ductility. The second phase particle dispersion is another way to improve the properties of W-based materials through the suppression of W grain growth and dispersion hardening. Nanocrystalline W with second phase particle dispersion could be one of the most promising methods to overcome the issues of W as PFMs.

Many research studies have been carried out on the synthesis of nanocrystalline W or W-based materials [1, 14, 17, 24–27]. A high-temperature sintering method was usually adopted to obtain high density W or W-based materials. The second phase particle dispersion is considered as one of the most promising methods to suppress the grain growth of W due to the blocking of GB movement through a pinning effect. However, nanocrystalline W was barely achieved as high temperature usually leads to the grain growth of W. Lee *et al*, prepared W with Vickers hardness ranging from 220 to 397 with grain sizes of 5.82–39.46 μm [24]. Xie *et al* prepared a W–Zr–Y₂O₃ alloy and the average grain size was 1.56 μm with a Vickers hardness of 520 in the rolling direction-transverse direction (RD-TD) and 516 in the rolling direction-normal direction (RD-ND) [25]. The Vickers hardness is one of the most important properties of W. Many research studies have reported that the Vickers hardness of W or W-based materials usually ranges from 231 to 729 with the grain size in the micrometer scale [24, 25, 28–34].

In a fusion reactor, W faces a high dose of low-energy He and fast neutron (14.1 MeV) irradiation, and the fast neutron irradiation will produce approximately 20–30 displacements per atom (dpa) every year [12, 35]. Furthermore, a great number of transmuted He atoms are produced through the nuclear transmutation caused by fast neutron irradiation. The He atoms coming from these two effects will result in the formation of He bubbles, which usually cause swelling and embrittlement of W [36–38]. Increasing GBs and interfaces can be an effective means of solving these problems as the GBs and interfaces are the ‘sinks’ to absorb and trap He atoms.

Qin *et al* reported that nanochannel structures in W films enhance radiation tolerance, and they revealed that abundant free surfaces of nanochannel W films act as efficient ‘sinks’ and quickly trap and release He atoms along the nanochannel [7]. Harrison *et al* studied the effect of He concentration and displacement damage on the microstructure of W and revealed

that the proportion of interstitial loops increase with the He-appm/dpa ratio, and this is attributed to the concomitant increase in bubble areal density [39]. El-Atwani *et al* studied He bubble formation in W under different extreme conditions and revealed that vacancy generation and migration are necessary conditions for enhanced trapping of He at GBs, thus demonstrating the importance of these phenomena for the radiation response of W materials with tailored grain size [17]. These research studies show the He bubble behavior of coarse and ultra-fine-grained W, or on the surface of samples (for example, transmission electron microscopy (TEM) foils). He bubble behavior of nanocrystalline bulk samples needs to be explored urgently. The irradiation tolerance performance of W with grain size smaller than 100 nm was very important and significant to study as nanocrystalline materials usually possess outstanding radiation tolerance due to their high volume fraction of GBs [21–23].

In this paper, nanocrystalline W-5 wt.% Y₂O₃ (WYO) with an average grain size of 10 nm was successfully fabricated for the first time by doping Y₂O₃ in W by resistance sintering under ultrahigh pressure (RSUHP) with the sintering temperature lower than the RCT. Moreover, higher density nanocrystalline W-5 wt.% Y₂O₃-2.5 wt.% Ni (WYON) with an average grain size smaller than 100 nm was designed by adding Ni into WYO and was successfully fabricated. Both sintered W-based materials exhibited ultrahigh hardness through the GB hardening and second phase particle dispersion hardening. High temperature He ion irradiation experiments on nanocrystalline WYO, WYON and ITER grade W with three irradiation doses were conducted to investigate their radiation tolerance in terms of He bubbles. A high substrate temperature during irradiation was adopted to increase the formation of He bubbles through the improvement of vacancies mobility [38, 40, 41]. Observations of bubble behavior at different dpa provide significant insights into the roles of GBs and phase boundaries (PBs) in enhancing radiation tolerance in nanocrystalline W-based alloys.

2. Experimental

2.1. Sample synthesis and preparation

WYO and WYON alloys were prepared by mechanical alloying followed by RSUHP. A high-energy ball mill method was adopted to grind the mixed initial powder. The purity of W, Y₂O₃ and Ni is larger than 99.9%, and the impurity of the initial powder is shown in table 1. The ball mill and grinding balls were made of WC with a ball-to-powder weight ratio of 30:1. The rotation speed was 500 rpm and the dry milling time was 4 h. The WYO and WYON powders were ball milled, respectively. Then, the ball-milled powder was formed into a powder compact by a hydraulic press with 960 MPa pressure, and the relative density of the powder compact was 56.6% for the WYO and 56.3% for the WYON. The prepared compacts were placed in a sintering mold and then subjected to ultrahigh pressure sintering for 3 h at a sintering temperature of 1000 °C and sintering pressure of 6 GPa. The ITER grade W was purchased from Antai Tianlong Tungsten Molybdenum

Table 1. The impurity content of the initial powder.

Powder	Maximum impurity content of element (wt. %)
W	Fe ≤ 0.004; Ag ≤ 0.002; Cu ≤ 0.003; Na ≤ 0.002; Ni ≤ 0.003; Si ≤ 0.002; C ≤ 0.01; O ≤ 0.04
Y ₂ O ₃	Fe ≤ 0.001; Ni ≤ 0.003; Ca ≤ 0.002; Na ≤ 0.004; Si ≤ 0.001; Pb ≤ 0.001; K ≤ 0.001; N ≤ 0.001; C ≤ 0.002; S ≤ 0.002
Ni	Fe ≤ 0.03; Co ≤ 0.01; Mg ≤ 0.009; Zn ≤ 0.002; Pb ≤ 0.002; Mn ≤ 0.003; Si ≤ 0.008; Ca ≤ 0.003; S ≤ 0.003; C ≤ 0.01; Cu ≤ 0.003; O ≤ 0.04

Technology Co., Ltd, and its purity was 99.9% with a relative density of 99.7%.

2.2. Density, hardness and ion irradiation of materials

The density of the sintered WYO, WYON and ITER grade W samples was characterized by a precision balance using the Archimedes drainage method. The sintered WYO, WYON and ITER grade W samples were polished to mirror surface using sandpaper first. The Vickers hardness of sintered material and ITER grade W was measured by the HV-1000IS Vickers hardness tester with a load of 200 g and holding time of 5 s. The high-temperature He⁺ ion irradiation experiments were conducted on NEC 400 kV ion implanter. The He⁺ ion energy was 120 keV and the doses were 2×10^{17} ions cm⁻², 5×10^{17} ions cm⁻² and 1×10^{18} ions cm⁻² with an irradiation temperature of 450 °C and dose rate of 4.85×10^{13} ions/cm²/s. The thermal stability of WYO and WYON is shown in supplementary material file, and Figure S2 show the result of rapid thermal annealing treatment.

2.3. Material characterization and data processing

The morphology and particle size of the initial powder were characterized by an FEI Nano SEM 430 field-emission scanning electron microscope (SEM). The microstructures of the initial powder, ball-milled powder and sintered bulk materials were characterized by a Panalytical model x-ray powder diffractometer (XRD). The surface of irradiated samples was coated with a Cu film of 530 nm in thickness at room temperature with a magnetic sputtering machine (MSP-3200H). The TEM samples of the unirradiated and irradiated WYO and WYON alloy and irradiated ITER grade W were prepared by a focused ion beam (FIB, FEI Strata DB 235). Ga ions with an accelerating voltage of 30 kV and beam current between 7000 pA to 50 pA were used to ion mill samples. The 10 kV low-energy Ga ions were adopted to clean the surface of the ion milled samples.

The sample of ITER grade W was cut into a 3 mm diameter disk after mechanically polishing down to 64 microns in thickness, and then the sample was polished using a twin-jet electro-polisher (Struers TenuPol-5) with a polishing solution of 0.5 wt.% NaOH aqueous solution at 10 V to make TEM specimen. The microstructure and grain size information were characterized by an FEI Tecnai F30 TEM using the bright-field images, dark-field images and high-resolution TEM (HRTEM) images. The mechanical polished sample of ITER grade W was electrochemically polished with 3 wt.% NaOH aqueous solution to make the SEM specimen. Nanomeasurer

software was used on the SEM images to obtain the particle size range and on the TEM images to obtain the grain size distribution, average grain size and medium grain size. Nanomeasurer software was also used to obtain the He bubble size distribution, average He bubble size and medium bubble size, and to obtain the diagonal length of the Vickers indentations of the sintered materials and ITER grade W material. The peak He concentration values were calculated using the Ion Distribution and Quick Calculation of Damage model in the stopping range of ions in matter (SRIM) (version 2013), and the peak He concentration values were about 13%, 33% and 66% for irradiation doses of 2×10^{17} ions cm⁻², 5×10^{17} ions cm⁻² and 1×10^{18} ions cm⁻², respectively.

3. Results and discussion

3.1. Fabrication and formation mechanisms of nanocrystalline WYO and WYON

Figure 1(a) shows the SEM image of the initial W powder, and the particles appear with spherical morphology with particle sizes ranging from 21 nm to 327 nm. Figure 1(b) shows the SEM image of the initial Y₂O₃ powder, and the particles appear with polyhedral morphology with particle sizes ranging from 20 to 116 nm. Figure 1(c) shows the SEM image of the initial Ni powder, and the particles appear with spherical morphology with particle sizes ranging from 22 to 354 nm. The initial powder was mixed and ball milled to refine the grain size. The ball-milled mixed powder was then sintered with the sintering temperature lower than the RCT of W to inhibit the grain growth. The holding time was set as 3 h to maximize the relative density of the bulk materials. Figures 2(a) and (c) show the bright-field TEM images of sintered WYO with different scale bars. Figures 2(b) and (d) are the corresponding dark-field images of figures 2(a) and (c), respectively, and the white areas are the grains of W in the (110) crystal direction. The selected area electron diffraction (SAED) pattern shown in the inset in figure 2(c) shows the nanocrystalline structure of sintered WYO. The statistical distribution of the grain size is shown in figure 2(e). The grain size of sintered WYO ranges from 3 to 89 nm with an average grain size (D_{ave}) of 10 nm and medium particle size (D_{50}) of 8 nm.

The grain growth was suppressed by the doping of Y₂O₃. Further investigation of the microstructure of sintered WYO was carried out to investigate the doping mode. Figure 3 shows the TEM and HRTEM images of sintered WYO alloy. The TEM image in figure 3(a) shows different nano-grains. The corresponding fast Fourier transformation (FFT) diffraction image at the bottom right of figure 3(a) confirms the existence

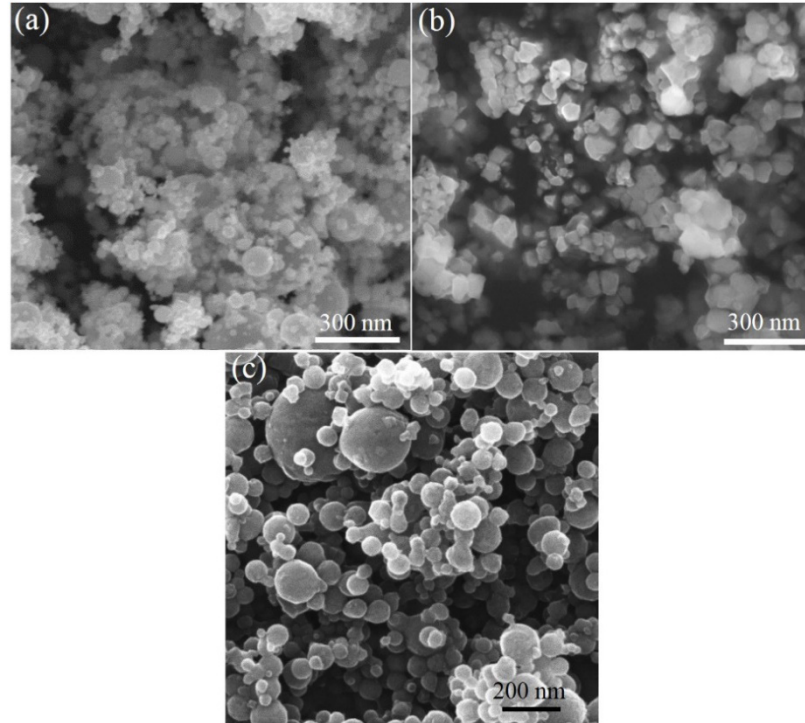


Figure 1. SEM images of initial (a) W powder, (b) Y_2O_3 powder and (c) Ni powder.

of nanocrystalline. Figure 3(b) is the HRTEM image that shows the W and Y_2O_3 nano-grains. The Y_2O_3 grains distribute between W (110) grains, and this is the intergranular doping mode. The corresponding fast Fourier transformation (FFT) diffraction image at the bottom right of figure 3(b) also confirms the existence of nanocrystalline. The GB between two W grains is a high-angle grain boundary (HAGB) with an orientation angle difference of 18.1° . The grain growth of W is suppressed by Y_2O_3 grains through the blocking of grain slipping.

Figure 4 shows the XRD patterns of the initial powder, ball-milled powder precursor and sintered bulk alloy of WYO. The initial W powder (black) possesses two phases: an α -W phase with a body-centered cubic structure (BCC), and β -W phase with an A15 cubic structure, and the diffraction peaks are marked with different crystal directions. The XRD pattern of the Y_2O_3 powder (red) possesses diffraction peaks from different crystal directions of Y_2O_3 powder. The XRD pattern of ball-milled WYO powder (deep blue) indicates that it only possesses the α -W phase, and this means that the β -W phase transforms into the α -W phase during the high-energy ball-milling process. The β -W phase possesses an A15 cubic structure, and it is a metastable structure with subharmonic energy. This β -W phase frequently transforms into a stable BCC structure whose Gibbs free energy is lower. The diffraction peaks of Y_2O_3 in ball-milled WYO are not observed as the relatively low doping content and weak signal of the second phase. The broadening of the W (110) Bragg peak of ball-milled WYO powder indicates the decrease in W grain size compared with the initial W powder grain size. The decrease in the full width at half maximum (FWHM) of sintered WYO in the W (110) Bragg peak represents the grain growth during the sintering process. The relative density of sintered WYO is 94.1%, shown in table 2.

Figures 5(a)–(d) are the TEM images of sintered WYON alloy. Figures 5(a) and (c) show the bright-field TEM image of sintered WYON with different scale bars. Figures 5(b) and (d) are the corresponding dark-field images of figures 5(a) and (c), respectively, and the white areas are the grains of W in the (110) crystal direction. The SAED pattern shown in the upper right corner shows the polycrystalline structure of sintered WYON. The statistical distribution of the grain size is shown in figure 5(e). The grain size of sintered WYON ranges from 12 to 199 nm with an average grain size (D_{ave}) of 85 nm and medium particle size (D_{50}) of 89 nm.

Figure 6 shows the HRTEM images of sintered WYON. Figure 6(a) of the HRTEM image shows the relationship between W, Ni and Y_2O_3 grains, and the crystal direction of the W grain is (110) with crystalline interplaner spacing of 0.2238 nm. The Ni (111) grain with crystalline interplaner spacing of 0.2034 nm and Y_2O_3 (222) grain with crystalline interplaner spacing of 0.3060 nm are next to the W (110) grains. The addition of Ni atoms activates the sintering process and promotes the density of bulk materials. The relative density of sintered WYON is 95.6%, as shown in table 2, and it is higher than the relative density of sintered WYO. The strategy to improve the density of W-based materials is shown in the supplementary material file, available online at stacks.iop.org/NF/59/106050/mmedia. Meanwhile, the addition of Ni makes it easy for W atoms at one crystal lattice to transfer to another crystal lattice or GBs between two W grains by reducing the grain growth activation energy. The addition of Ni will promote the densification and grain growth of bulk material. Furthermore, the Y_2O_3 grain with crystalline interplaner spacing of 0.2034 nm in the (310) crystal direction was found in figure 6(a). Figure 6(b) shows the HRTEM image of two W grains in the (110) crystal direction with crystalline

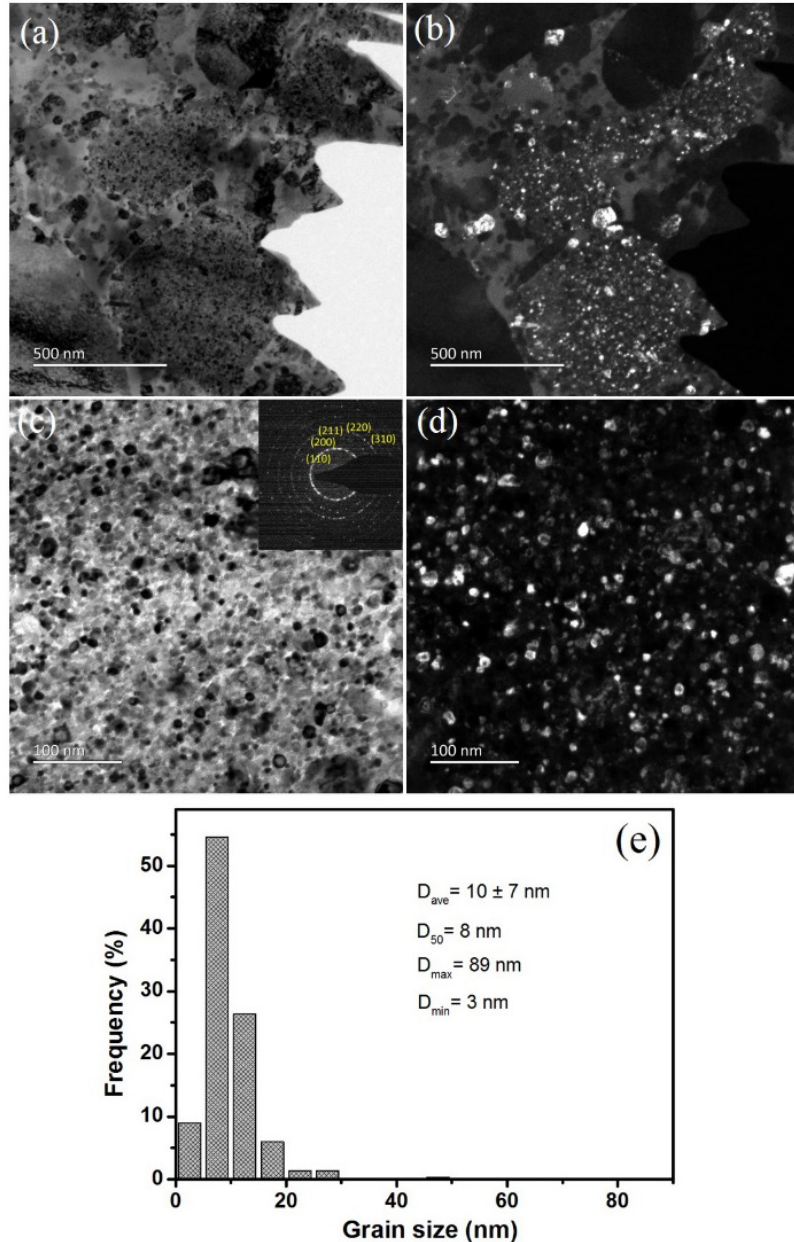


Figure 2. (a) and (c) bright-field TEM images of sintered WYO; (b) and (d) corresponding dark-field TEM images of sintered WYO; (e) grain size statistical distribution of sintered WYO.

interplaner spacing of 0.2238 nm. The GB between two grains is a HAGB with an orientation angle difference of 13.3°.

Figure 7 shows the XRD patterns of the initial powder, ball-milled powder precursor and sintered bulk WYON alloy. The XRD patterns of the initial W powder (black) and the Y₂O₃ powder (red) show that they possess the same features as those in figure 3. The Ni powder (deep blue) possesses face-centered cubic (FCC) structure with three diffraction peaks. The ball-milled WYON powder (magenta) only possesses the α -W phase, and this means the β -W phase transforms into the α -W phase during the high-energy ball-milling process due to the same reason described in the previous paragraphs. The diffraction peaks of Y₂O₃ and Ni in ball-milled WYON are not observed. The broadening of W (110) Bragg peaks of ball-milled WYON powder signifies the refinement of W

grains from the initial powder. The decrease in the FWHM of sintered WYON signifies the grain growth during the sintering process.

3.2. Ultrahigh hardness of nanocrystalline WYO and WYON

Table 2 Shows the relative density, average grain size, GB volume fraction and Vickers hardness of sintered alloys and ITER grade W. Figure 8(a) shows one representative SEM image of ITER grade W and figure 8(b) shows one representative TEM image of ITER grade W. The density of ITER grade W bulk is 99.7% with an average grain size of 2296 nm. The average grain size was obtained from the grain size statistical distribution shown in figure 8(c) based on TEM images of ITER grade W.

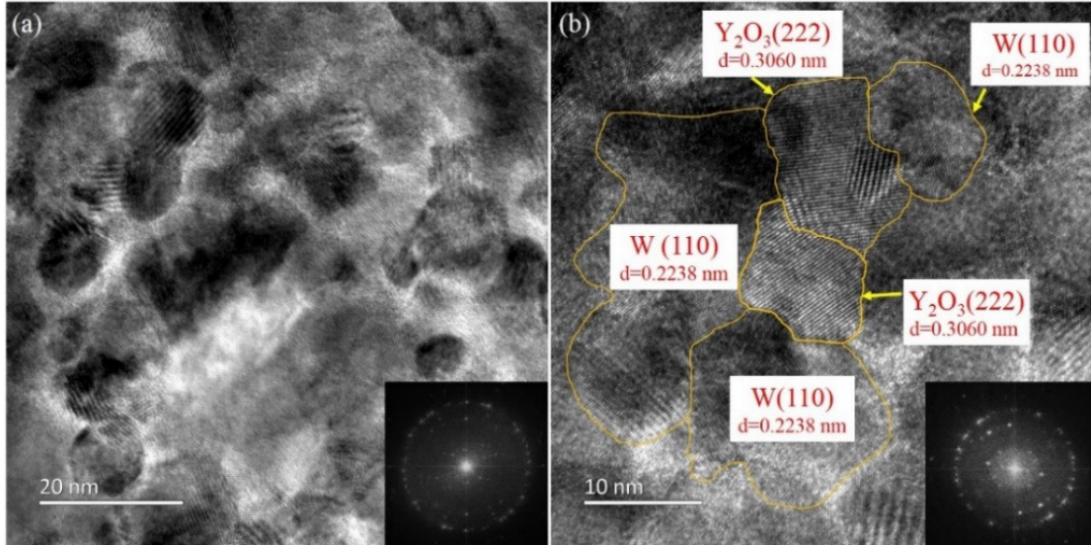


Figure 3. (a) TEM image and (b) HRTEM image of sintered WYO.

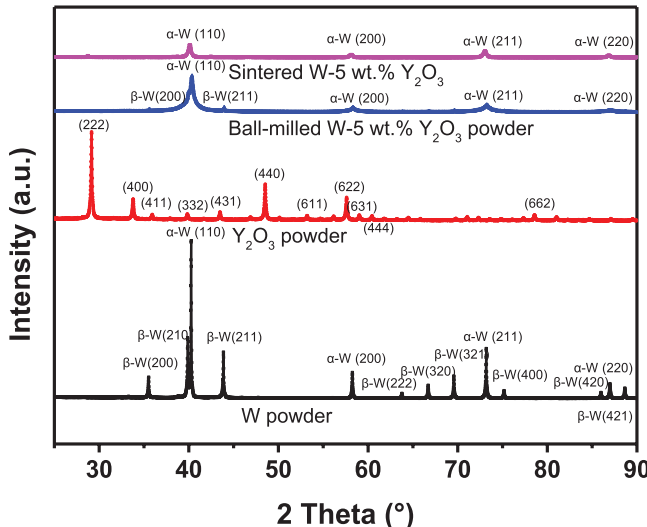


Figure 4. XRD patterns of initial W, Y_2O_3 powder, ball-milled WYO powder and sintered WYO bulk alloy.

The Vickers hardness of sintered WYO alloy is 1909.3 (18.71 GPa), which is about four times higher than that of the ITER grade W bulk. The Vickers hardness of ITER grade W is 486.8 (4.77 GPa). The higher hardness of sintered WYO is believed to come from the smaller grain size of W and doped Y_2O_3 . The doping of Y_2O_3 particles disperses between W grains and suppresses the grain growth of W grains. The Vickers hardness of sintered WYON alloy is 1292.2 (12.66 GPa), which is 2.65 times higher than that of ITER grade W. The addition of Ni activates the sintering of ball-milled powder, and leads to the grain growth compared with sintered WYO. The Vickers hardness of sintered WYON is smaller than that of sintered WYO as its grain size is larger than the WYO grain size.

The reduction in grain size, d , causes the increase in GB volume fraction, V_{gb} , which follows the relationship $V_{gb} = 1 - \left(\frac{d-t}{d}\right)^3$, where t is the mean GB thickness, and the GB usually possesses three atoms [42]. The atomic radius of W is 0.137 nm, and the GB thickness of W is 0.822 nm. The

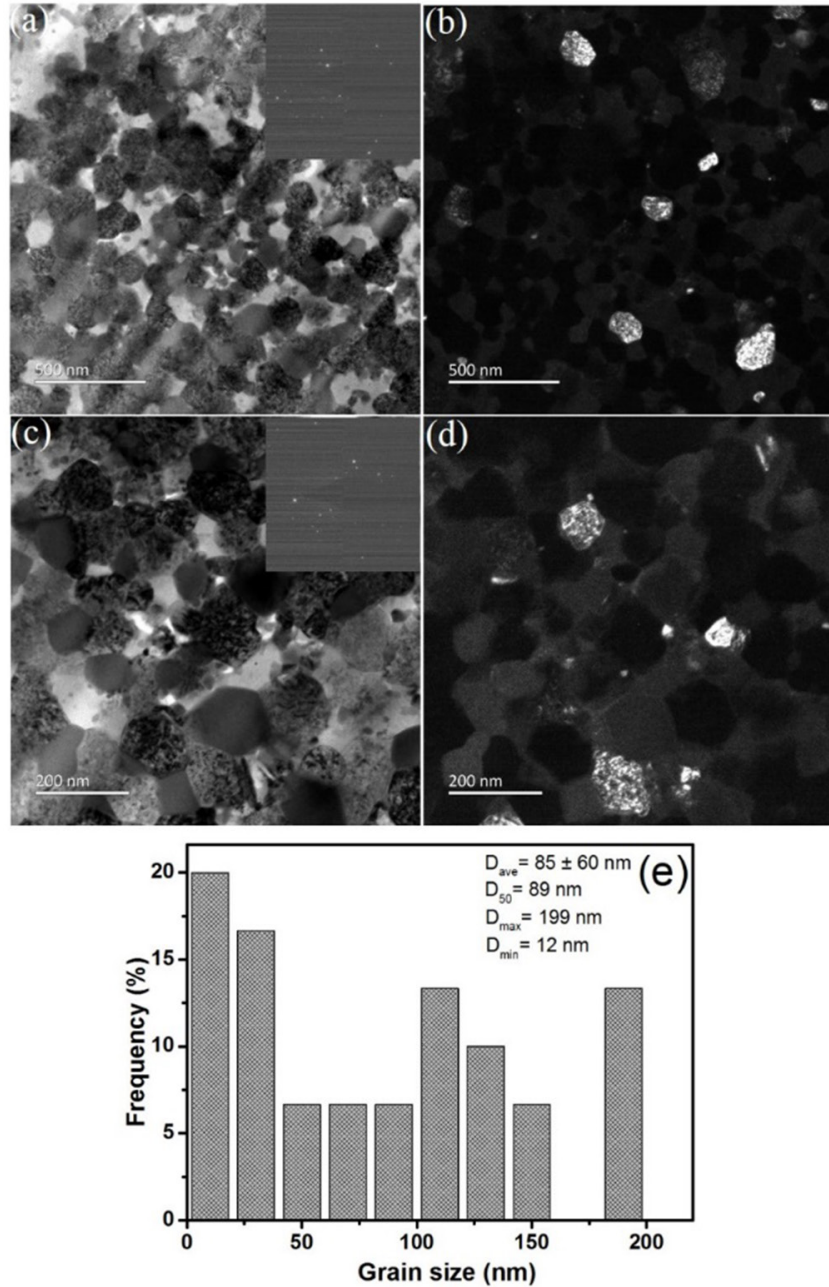
average grain size of sintered WYO is 10 nm, and the V_{gb} is about 27.0%. The average grain size of sintered WYON is 85 nm, and the V_{gb} is about 5.97%. The average grain size of ITER grade W is 2296 nm, and the V_{gb} is about 0.125%. The GB hardening originates from the high volume fraction of GBs and the dispersion of the second phase. The essence of the GB hardening mechanism is to prevent the movement of dislocations in the grains. The dislocations on the deformed grain slip surface are often stacked in front of the GB or the sub-GB to form a dislocation cluster. Dislocation clusters are formed when dislocations encounter obstacles in motion and external forces are insufficient to overcome obstacles. The smaller the grain size, the more GBs, the greater the resistance to dislocation motion.

Second phase particle pinning acts to pin the GBs and prevent GB sliding, and this is called dispersion strengthening of second phase particles. Figure 9 shows the plot of Vickers hardness as a function of grain size of W/W-based materials. Many research studies have reported that the Vickers hardness of coarse-grained W/W-based materials is between 292 to 587 with the micrometer-scaled grains. A W-5 wt.% Y_2O_3 alloy with ultra-fine grains of 550 nm was fabricated by Dong *et al* [43], and the Vickers hardness was 729.1. The highest hardness of W-based materials in figure 9 was obtained by this work, which has a grain size smaller than 100 nm. The nanocrystalline W-based alloys in current study and marked by red circle in figure 9 possess such high Vickers hardness that has never been reported.

Figure 10 shows the SEM images of Vickers indents and schematic diagrams of the indentation process of (a) ITER grade W, (b) sintered WYO and (c) sintered WYON. The indents show four pyramid morphology and different indentation depths (or sizes) for different samples with the same load of 200 g. The diagonal lengths D1 and D2 of sintered alloy and ITER grade W were measured by Nanomeasurer software and marked in the bottom left of the SEM images, respectively. The higher Vickers hardness of samples with smaller diagonal lengths D1 and D2 are due to the greater resistance of dislocation motion through GB hardening and dispersion hardening.

Table 2. Relative density, average grain size, GB volume fraction and Vickers hardness of sintered bulk alloys and ITER grade W.

Materials	Relative density (%)	Average grain size (nm)	V_{gb} (%)	HV_{200g} (kgf mm^{-2})/(GPa)
Sintered WYO	94.1 ± 0.6	10 ± 7	27.0 ± 9.96	$1909.3 \pm 65.3/18.71 \pm 0.64$
Sintered WYON	95.6 ± 0.6	85 ± 60	5.97 ± 5.46	$1292.2 \pm 31.2/12.66 \pm 0.31$
ITER grade W	99.7 ± 0.2	2296 ± 870	0.125 ± 0.057	$486.8 \pm 12.5/4.77 \pm 0.12$

**Figure 5.** (a) and (c) bright-field TEM images of sintered WYON; (b) and (d) corresponding dark-field TEM images of sintered WYON; and (e) grain size statistical distribution of sintered WYON.

The schematic diagram shows that the GB hardening is through dislocation pileup and the dispersion strengthening is through second phase particle pinning acting to pin the GBs and prevent GB sliding. The sintered WYO possesses smaller grain size and more dislocation pileups during the indentation process. Furthermore, the motion of dislocations is impeded by second phase particles of Y_2O_3 (yellow circle spots), and

this leads to higher hardness. The sintered WYON has a grain size of 85 nm, and the dislocation pileups that occurred are less than those in the WYO. The second phase particles of Y_2O_3 (yellow circle spots) and Ni (orange circle spots) impede the motion of dislocations, and the force is small because of the large grain of the Y_2O_3 and Ni. These factors lead to the lower hardness of sintered WYON (compared with sintered

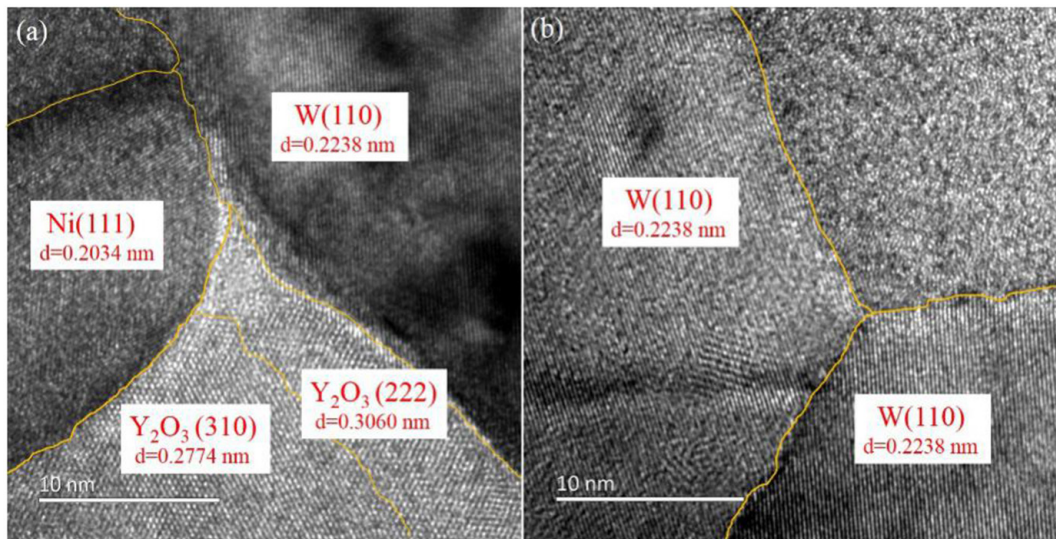


Figure 6. HRTEM images of sintered WYON showing (a) the relationship of W, Ni and Y_2O_3 grains, and (b) the relationship of W and W grains.

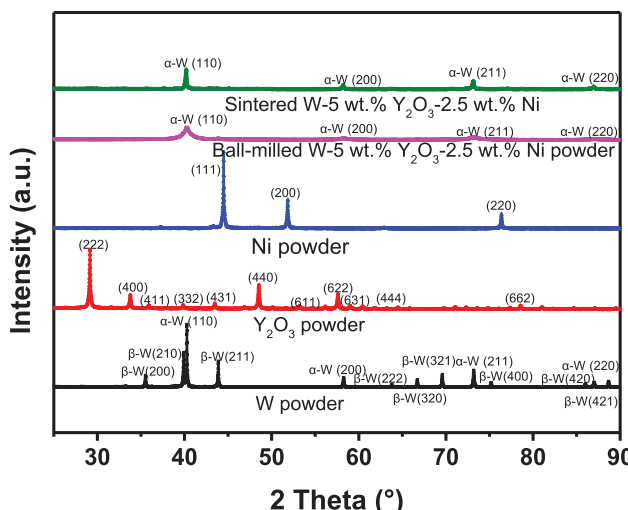


Figure 7. XRD patterns of initial W, Ni and Y₂O₃ powder, ball-milled WYON powder and sintered WYON bulk material.

WYO). The Vickers hardness of ITER grade W is 4.77 GPa as the average grain size is 2296 nm, and the dislocation pileups that occurred are much less than those in the sintered WYO and WYON.

3.3. Exceptional radiation tolerance of nanocrystalline WYO and WYON

Figure 11 shows the low magnification bright-field TEM images of 120 keV He⁺ ion irradiated W, WYO and WYON samples at different doses. All the TEM images were obtained at the same defocus value. The Cu film was coated on an irradiated sample surface, and then the Pt film was coated on the Cu film during the FIB process. The Cu film and Pt films were used to protect the surface of irradiated samples during sample preparation, and all the irradiated areas of the irradiated samples are retained during the FIB process. Figure 11(a) shows the irradiated ITER grade W at an irradiation dose of 2×10^{17} ions cm⁻², and it shows a representative image that indicates the relative position of the Cu film, Pt film and sample. All

the sample surfaces are marked with red arrows in figure 11. The He bubble number increases with the increase in depth, and reaches a peak at depths of 258 nm, 300 nm and 306 nm for W, WYO and WYON, respectively, and then decreases to zero at depths of 534 nm, 570 nm and 585 nm for W, WYO and WYON, respectively.

To further study the influence of different irradiation doses on irradiated samples with different grain sizes, the high magnification bright-field TEM images of peak damaged regions are presented in figure 12. All the TEM images in figure 12 show the existence of He bubbles. The He bubbles become larger for each sample with the increase in irradiation dose due to the fact that the He bubbles interact with the incident He atoms and absorb the incident He atoms. The He ion irradiation is followed by a diffusion phase with a probable growth mechanism—coalescence of the bubbles. In addition, the presence of irradiation gaps can induce accelerated diffusion through irradiation. Another reason is that the high-temperature irradiation promotes the formation and diffusion of vacancies, and the vacancies provide more positions for incident He atoms.

The TEM images of samples irradiated at the same irradiation dose show that the He bubble density increases with the increase in grain size. The He bubble density of ITER grade W is larger than that of the nanocrystalline WYO and WYON, and it is shown in figure 12 and is illustrated by comparison of bubble areal density in figure 13(a). This means that many more GBs and PBs in nanocrystalline WYO and WYON effectively reduce the radiation damage. The V_{gb} of ITER grade W is only 0.125%, and only a small fraction of He bubbles are trapped in GBs; the majority of the He bubbles are distributed in the interior of the grains shown in figures 12(a), (d) and (g). Figures 12(a) and (b) show that some He bubbles are concentrated on the GBs in W, and the He bubbles become larger as the irradiation dose increases. The He bubbles are concentrated to form many bubble lines in the W sample with the irradiation dose of 1×10^{18} ions cm^{-2} , as shown in figure 12(c).

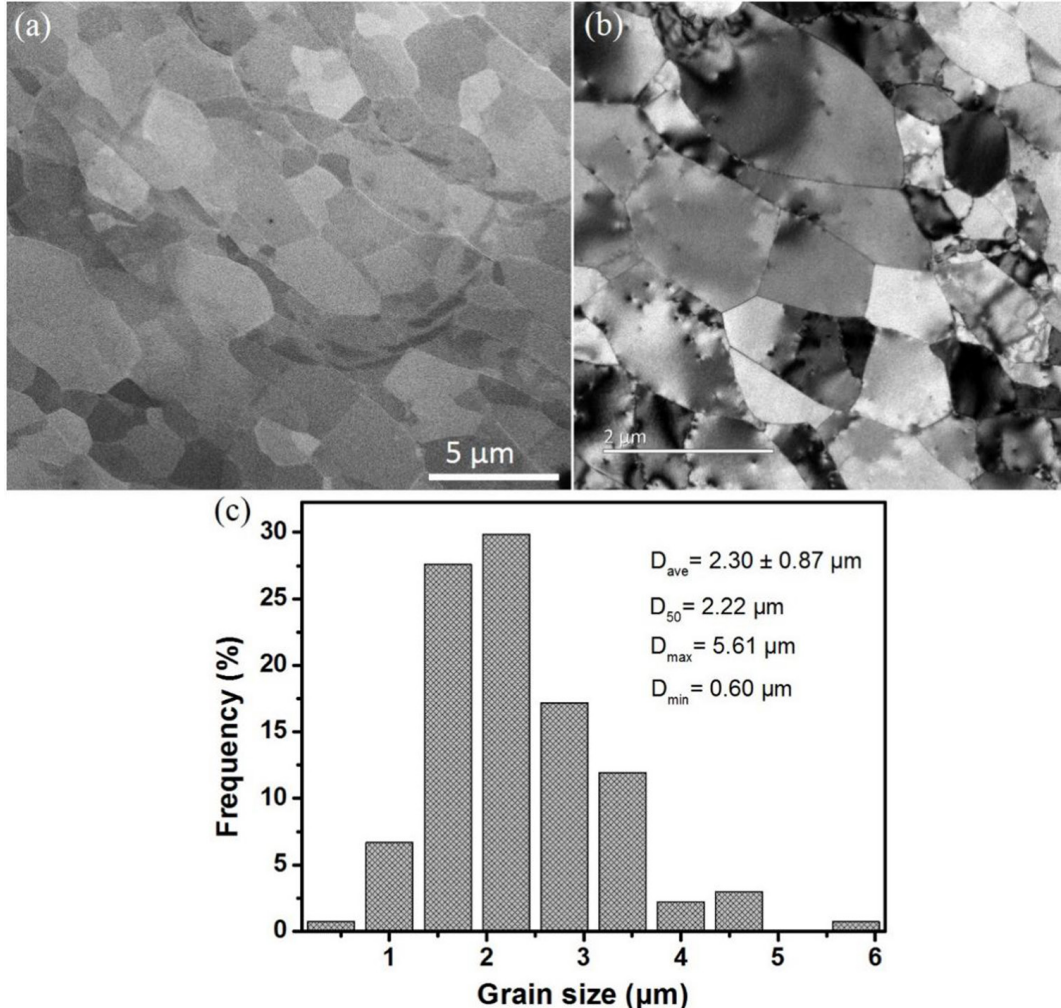


Figure 8. (a) SEM image, (b) TEM image and (c) the grain size statistical distribution of ITER grade W.

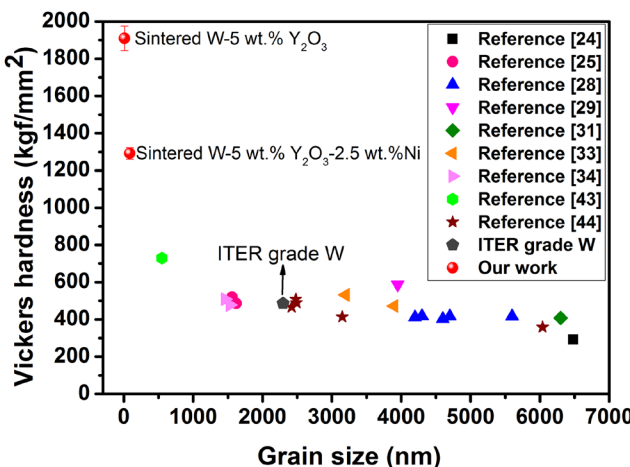


Figure 9. A Vickers hardness versus grain size curve of W/W-based materials [24, 25, 28, 29, 31, 33, 34, 43, 44].

The PBs play important roles in irradiation tolerance, and the volume fraction of PBs is defined as V_{pb} . The V_{gb} and V_{pb} of WYO are 27.0% and 5.19%, respectively, and it provides many He bubble ‘sinks’. He bubbles are trapped by the GBs and PBs, as shown in figures 12(d)–(f), and no bubble lines are formed, even at the highest irradiation dose

of 1×10^{18} ions cm⁻². The V_{gb} and V_{pb} of WYON are 5.97% and 1.47%, respectively, and the He atom absorbing ability of the GBs is limited. The little He bubbles are trapped by the GBs and PBs, and many other He bubbles are distributed in the interior of grains. Little bubble lines are formed at the irradiation dose of 1×10^{18} ions cm⁻² shown in figure 12(i). TEM images at higher magnification at other irradiated areas are shown in figure S1

The He bubble areal density and average bubble size are obtained from the TEM images through the statistics of the He bubble’s number and size. The TEM images are selected from different depths of irradiation areas. All the He bubbles in the TEM images are counted and the sizes are measured to reduce the statistical error, and the He bubble numbers range from 846 to 4880. Figure 13 shows the comparisons of bubble areal density and average bubble size as a function of irradiation dose for 120 keV He⁺ irradiated samples at 450 °C. The He bubble size and density increases with the increase in irradiation dose for irradiated W, WYON and WYO, respectively. In figure 13(a), the He bubble density of WYON and WYO is lower than that of ITER grade W at the same irradiation dose. The bubble areal density of WYON is 1.17×10^{16} m⁻² at the irradiation dose of 2×10^{17} ions cm⁻². With the same radiation dose of 2×10^{17} ions cm⁻², the bubble areal density

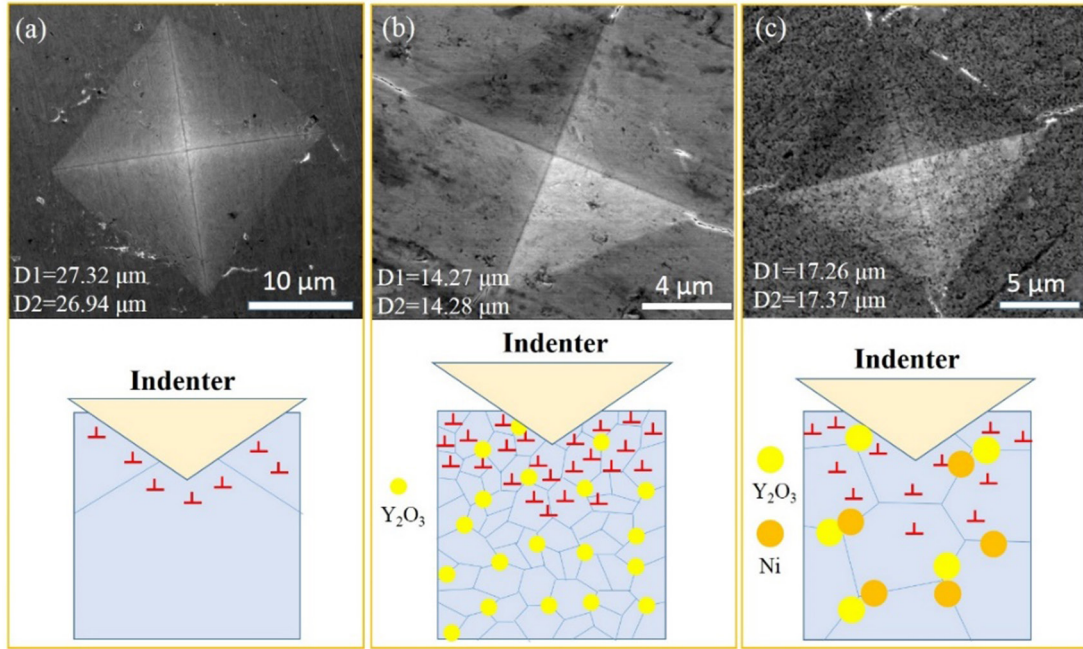


Figure 10. SEM images of Vickers indentation and schematic diagrams of the indentation process of (a) ITER grade W, (b) sintered WYO and (c) sintered WYON. The schematic diagram shows the GB hardening through dislocation pileup and the dispersion strengthening by second phase particle pinning that acts to pin the GBs and prevent GB sliding. The yellow circle spots represent the Y₂O₃ grains, and the orange circle spots represent the Ni grains. Here, ‘+’ represents the dislocations.

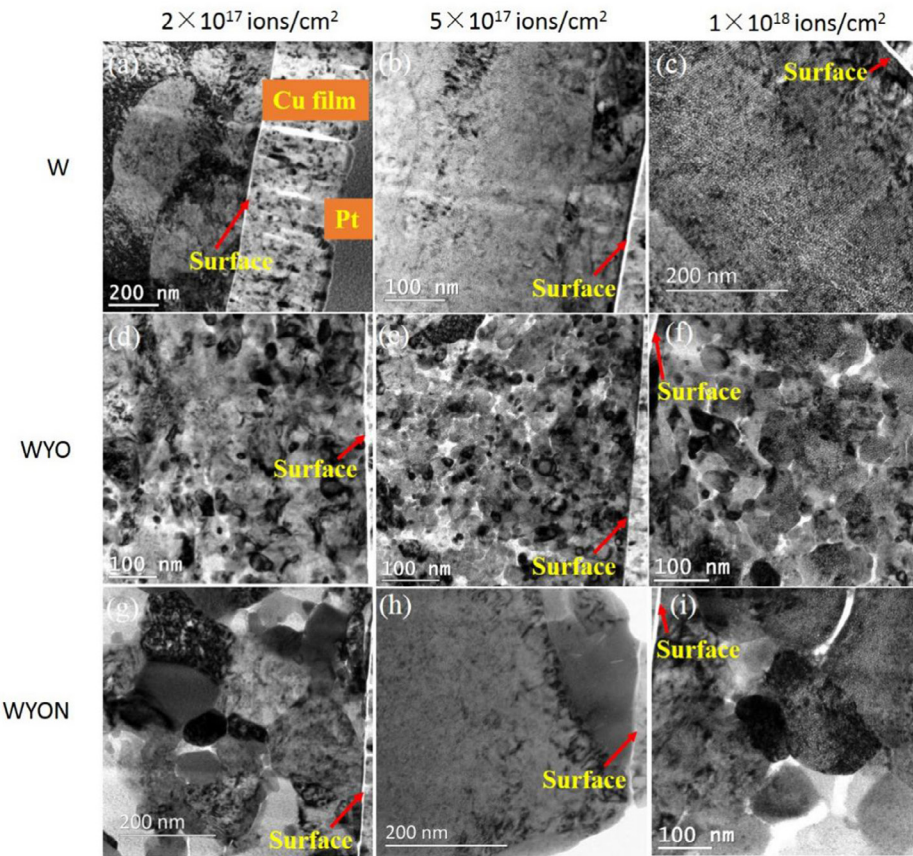


Figure 11. Low magnification bright-field TEM images of 120 keV He⁺ irradiated samples at different doses: (a) W, 2×10^{17} ions cm⁻²; (b) W, 5×10^{17} ions cm⁻²; (c) W, 1×10^{18} ions cm⁻²; (d) WYO, 2×10^{17} ions cm⁻²; (e) WYO, 5×10^{17} ions cm⁻²; (f) WYO, 1×10^{18} ions cm⁻²; (g) WYON, 2×10^{17} ions cm⁻²; (h) WYON, 5×10^{17} ions cm⁻²; and (i) WYON, 1×10^{18} ions cm⁻².

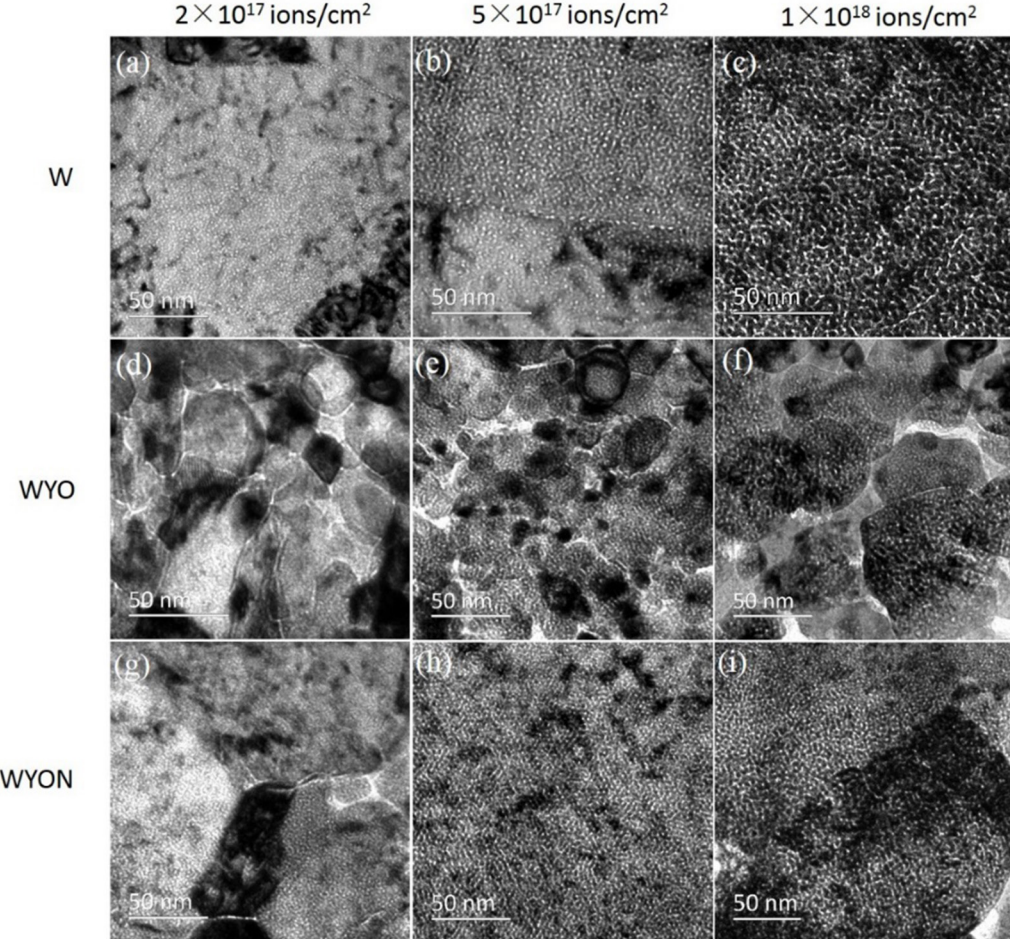


Figure 12. High magnification bright-field TEM images of 120 keV He^+ irradiated samples at different doses that show He bubbles: (a) W, 2×10^{17} ions cm^{-2} ; (b) W, 5×10^{17} ions cm^{-2} ; (c) W, 1×10^{18} ions cm^{-2} ; (d) WYO, 2×10^{17} ions cm^{-2} ; (e) WYO, 5×10^{17} ions cm^{-2} ; (f) WYO, 1×10^{18} ions cm^{-2} ; (g) WYON, 2×10^{17} ions cm^{-2} ; (h) WYON, 5×10^{17} ions cm^{-2} ; and (i) WYON, 1×10^{18} ions cm^{-2} . All TEM images are obtained at the same defocus value to reduce the statistical error.

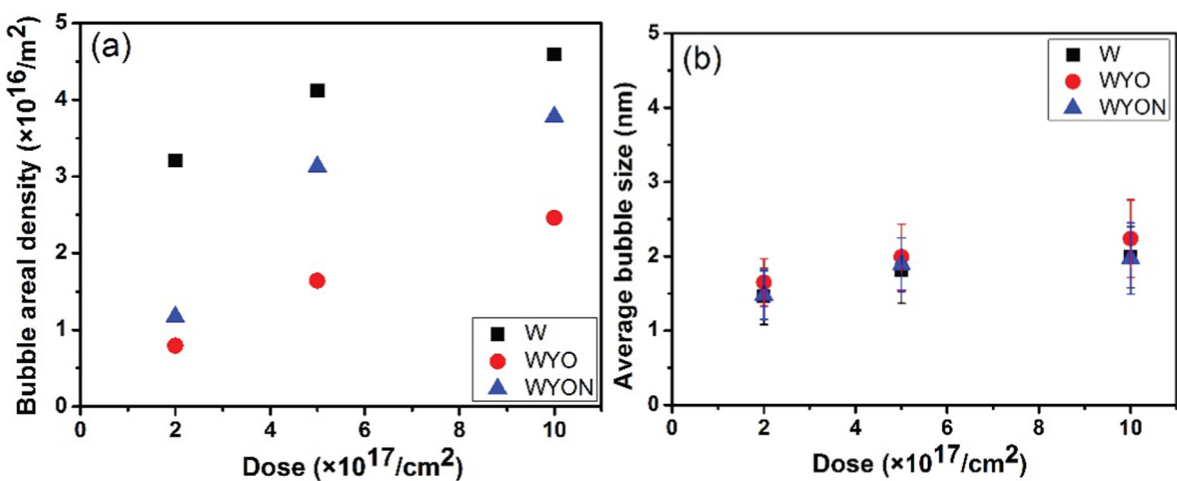


Figure 13. Comparisons of (a) bubble areal density and (b) average bubble size as a function of irradiation dose for 120 keV He^+ irradiated samples at 450 °C. Error bars are included to indicate the statistical errors of the bubble sizes.

of WYO is $7.94 \times 10^{15} \text{ m}^{-2}$, and this is about four times smaller than that in ITER grade W ($3.21 \times 10^{16} \text{ m}^{-2}$) due to the smaller grain size of WYO. The bubble areal density of W, WYON and WYO increases with the irradiation dose, respectively, and the bubble areal density of WYO and WYON are

still smaller than that of ITER grade W at a higher dose. The bubble areal densities of W, WYO and WYON are related to the grain size and thus volume fraction, which plays an important role in the absorption and transportation of He bubbles. A larger volume fraction of GBs and PBs reduces the bubble

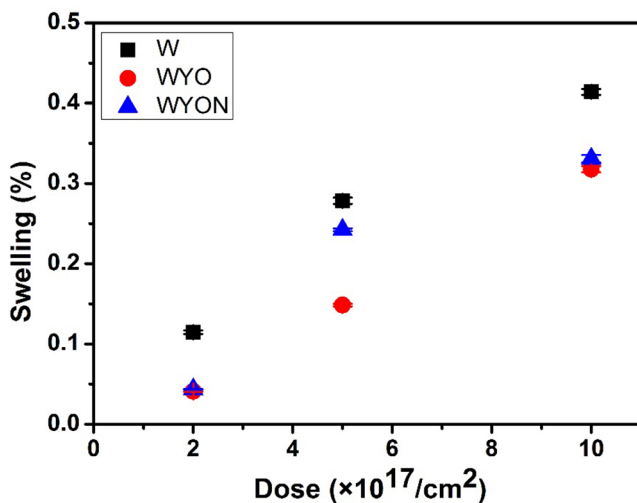


Figure 14. Comparisons of He bubble-induced swelling as a function of irradiation dose for 120 keV He^+ irradiated samples at 450 °C. Error bars are included to indicate the statistical and calculated errors.

areal density of He bubbles more. Figure 13(b) shows that the average bubble size slightly increases with the increase in irradiation dose. The average He bubble size of WYO is slightly larger than that of ITER grade W and WYON at the highest dose.

Figure 14 shows the comparisons of He bubble-induced swelling as a function of irradiation dose for 120 keV He^+ irradiated samples at 450 °C. The He bubble-induced swelling is calculated by the formula $s = q/(1 - q)$, where q is the volume ratio of all He bubbles to the irradiated TEM sample. All He bubbles are regarded as spherical shape, and the volume of He bubbles is calculated by $4\pi r^3/3$, where r is the radius of the He bubbles. The volume of irradiated TEM samples is calculated by the product of the area and the thickness of the TEM sample. The average thickness of the irradiated TEM sample is 45.7 nm, measured at the sample surface from high resolution SEM images. The results show that the swelling value increases with the increase in irradiation dose for ITER grade W, nanocrystalline WYO and nanocrystalline WYON, respectively. The swelling value of nanocrystalline WYO and WYON is smaller than that in ITER grade W for three irradiation doses, and increases with the increase in grain size. The swelling values of nanocrystalline WYO and WYON are 0.0409% and 0.0435%, respectively, and the swelling value of nanocrystalline WYO is about three times smaller than that of ITER grade W at the irradiation dose of 2×10^{17} ions cm^{-2} . Nanocrystalline WYO and WYON possess smaller grain sizes and large volume fractions of GBs and PBs. The He atoms can be easily concentrated on the GBs and PBs as there are many vacancies in the GBs and PBs; thus, the He atoms occupy the vacancies in the GBs and PBs to form He bubbles. Therefore, it is reasonable to conclude that the nanocrystalline WYO and WYON have excellent He irradiation tolerance compared with ITER grade W, and the large volume fraction of GBs and PBs provides positions for the absorption of He bubbles.

Conclusions

In summary, nanocrystalline WYO with an average grain size of 10 nm and WYON with an average grain size of 85 nm were successfully fabricated for the first time using a high-energy ball-milling method followed by RSUHP at 1000 °C for 3 h. Different dose He^+ ion irradiation experiments for WYO, WYON and ITER grade W were conducted using 120 keV He^+ ions at 450 °C. Investigation of the microstructure of sintered WYO shows that the intergranular doping of Y_2O_3 grains is between W grains, and the doping of Y_2O_3 suppresses the grain growth of W grains. The addition of Ni atoms maximizes the density of the material by activating the sintering process. The hardness of sintered WYO is 1909.3 (18.71 GPa), the hardness of sintered WYON is 1292.2 (12.66 GPa), and the hardness of both is much higher than that of ITER grade W. The higher hardness of sintered WYO and sintered WYON comes from the GB hardening through dislocation pileup and dispersion strengthening due to second phase particle pinning acting to pin the GBs and prevent GB sliding. A remarkable irradiation tolerance of WYO and WYON in terms of He bubbles was reported when compared to ITER grade W. The He bubble areal densities and swelling values of WYO and WYON are lower than those of ITER grade W at all irradiation doses. WYO with a grain size of 10 nm possesses exceptional irradiation tolerance compared to 85 nm WYON and coarse-grained 2296 nm ITER grade W. Investigations of the microstructure of irradiated samples show that the GBs and PBs act as ‘sinks’ for He atoms. The large volume fractions of GBs and PBs possess many vacancies and improve the absorption of He bubbles. Nanocrystalline W-based alloy is testified to be a promising material for resisting He ion irradiation damage, and a potential solution for solving the issues associated with W as PFMs in fusion reactors.

Acknowledgments

This work was supported by the National Magnetic Confinement Fusion Energy Research Project from the Ministry of Science and Technology of China (Grant Nos. 2015GB121004, 2017YFE0302500 and 2018YFE0307100), the National Key R&D Program of China (Grant No. 2016YFA0401503), the Youth Innovation Promotion Association of CAS (2016006), and the National Science and Foundation of China (NSFC) (Grant Nos. 11575288, 51402350, 11375018 and 11528508). E.F. appreciates the support from the China-Romania Science and Technology Cooperation Committee 43rd Regular Meeting Exchange Program, the Ion Beam Materials Lab at Peking University and the Instrumental Analysis Fund of Peking University.

Competing financial interests

The authors declare no competing financial interest.

References

- [1] El-Atwani O., Esquivel E., Efe M., Aydogan E., Wang Y.Q., Martinez E. and Maloy S.A. 2018 Loop and void damage during heavy ion irradiation on nanocrystalline and coarse grained tungsten: microstructure, effect of dpa rate, temperature, and grain size *Acta Mater.* **149** 206–19
- [2] Zhao M., Liu F., Yang Z., Xu Q., Ding F., Li X., Zhou H. and Luo G.-N. 2018 Fluence dependence of helium ion irradiation effects on the microstructure and mechanical properties of tungsten *Nucl. Instrum. Methods B* **414** 121–5
- [3] Petti D.A., McCarthy K.A., Gulden W., Piet S.J., Seki Y. and Kolbasov B. 1996 An overview of safety and environmental considerations in the selection of materials for fusion facilities *J. Nucl. Mater.* **233–7** 37–43
- [4] Davis J.W., Barabash V.R., Makhankov A., Plochl L. and Slattery K.T. 1998 Assessment of tungsten for use in the ITER plasma facing components *J. Nucl. Mater.* **258–63** 308–12
- [5] Qin W., Wang Y., Tang M., Ren F., Fu Q., Cai G., Dong L., Hu L., Wei G. and Jiang C. 2018 Microstructure and hardness evolution of nanochannel W films irradiated by helium at high temperature *J. Nucl. Mater.* **502** 132–40
- [6] Huang L., Jiang L., Topping T.D., Dai C., Wang X., Carpenter R., Haines C. and Schoenung J.M. 2017 *In situ* oxide dispersion strengthened tungsten alloys with high compressive strength and high strain-to-failure *Acta Mater.* **122** 19–31
- [7] Qin W., Ren F., Doerner R.P., Wei G., Lv Y., Chang S., Tang M., Deng H., Jiang C. and Wang Y. 2018 Nanochannel structures in W enhance radiation tolerance *Acta Mater.* **153** 147–55
- [8] Tazhibayeva I. et al 2017 Study of properties of tungsten irradiated in hydrogen atmosphere *Nucl. Fusion* **57** 126062
- [9] Hammond K.D., Blondel S., Hu L., Maroudas D. and Wirth B.D. 2018 Large-scale atomistic simulations of low-energy helium implantation into tungsten single crystals *Acta Mater.* **144** 561–78
- [10] Yao G., Tan X.-Y., Luo L.-M., Zan X., Liu J.-Q., Xu Q., Zhu X.Y. and Wu Y.-C. 2018 Repair behavior of He⁺-irradiated W-Y₂O₃ composites after different temperature-isochronal annealing experiments *Nucl. Instrum. Methods B* **415** 82–8
- [11] Das S., Armstrong D.E.J., Zayachuk Y., Liu W., Xu R. and Hofmann F. 2018 The effect of helium implantation on the deformation behaviour of tungsten: x-ray micro-diffraction and nanoindentation *Scr. Mater.* **146** 335–9
- [12] Philipp V. 2011 Tungsten as material for plasma-facing components in fusion devices *J. Nucl. Mater.* **415** S2–9
- [13] Smid I., Akiba M., Vieider G. and Plochl L. 1998 Development of tungsten armor and bonding to copper for plasma-interactive components *J. Nucl. Mater.* **258–63** 160–72
- [14] Mathaudhu S.N., DeRosset A.J., Hartwig K.T. and Kecske L.J. 2009 Microstructures and recrystallization behavior of severely hot-deformed tungsten *Mater. Sci. Eng. A* **503** 28–31
- [15] Kong X.-S., Hou J., Li X.L., Wu X., Liu C.S., Chen J.L. and Luo G.-N. 2017 First principles study of inert-gas (helium, neon, and argon) interactions with hydrogen in tungsten *J. Nucl. Mater.* **487** 128–34
- [16] Sand A.E., Nordlund K. and Dudarev S.L. 2014 Radiation damage production in massive cascades initiated by fusion neutrons in tungsten *J. Nucl. Mater.* **455** 207–11
- [17] El-Atwani O., Hattar K., Hinks J.A., Greaves G., Harilal S.S. and Hassanein A. 2015 Helium bubble formation in ultrafine and nanocrystalline tungsten under different extreme conditions *J. Nucl. Mater.* **458** 216–23
- [18] Meyers M.A., Mishra A. and Benson D.J. 2006 Mechanical properties of nanocrystalline materials *Prog. Mater Sci.* **51** 427–556
- [19] Senthilnathan N., Annamalaia A.R. and Venkatachalam G. 2018 Microstructure and mechanical properties of spark plasma sintered tungsten heavy alloys *Mater. Sci. Eng. A* **710** 66–73
- [20] Li X.B., Zhu D.H., Li C.J. and Chen J.L. 2017 Cracking and grain refining behaviors of tungsten based plasma facing materials under fusion relevant transient heat flux *Fusion Eng. Des.* **125** 515–20
- [21] Cheng G.M., Xu W.Z., Wang Y.Q., Misra A. and Zhu Y.T. 2016 Grain size effect on radiation tolerance of nanocrystalline Mo *Scr. Mater.* **123** 90–4
- [22] Yu K.Y., Liu Y., Sun C., Wang H., Shao L., Fu E.G. and Zhang X. 2012 Radiation damage in helium ion irradiated nanocrystalline Fe *J. Nucl. Mater.* **425** 140–6
- [23] Park N.-Y., Cha P.-R., Kim Y.-C., Seok H.-K., Han S.-H., Lee S.-C., Cho S. and Jung H. 2009 Radiation damage in nano-crystalline tungsten: a molecular dynamics simulation *Met. Mater. Int.* **15** 447–52
- [24] Lee G., McKittrick J., Ivanov E. and Olevsky E.A. 2016 Densification mechanism and mechanical properties of tungsten powder consolidated by spark plasma sintering *Int. J. Refract. Met. Hard Mater.* **61** 22–9
- [25] Xie Z.M., Liu R., Zhang T., Fang Q.F., Liu C.S., Liu X. and Luo G.N. 2016 Achieving high strength/ductility in bulk W-Zr-Y₂O₃ alloy plate with hybrid microstructure *Mater. Des.* **107** 144–52
- [26] Autissier E., Richou M., Minier L., Naimi F., Pintsuk G. and Bernard F. 2014 Spark plasma sintering of pure and doped tungsten as plasma facing material *Phys. Scr. T* **159** 014034
- [27] Ren C., Zak Fang Z., Zhang H. and Koopman M. 2016 The study on low temperature sintering of nano-tungsten powders *Int. J. Refract. Met. Hard Mater.* **61** 273–8
- [28] Zhang L.H., Jiang Y., Fang Q.F., Zhang T., Wang X.P. and Liu C.S. 2016 Toughness and microstructure of tungsten fibre net-reinforced Tungsten composite produced by spark plasma sintering *Mater. Sci. Eng. A* **659** 29–36
- [29] Qina M., Chena Z., Chen P., Zhao S., Li R., Ma J. and Qu X. 2017 Fabrication of tungsten nanopowder by combustion-based method *Int. J. Refract. Met. Hard Mater.* **68** 145–50
- [30] El-Atwani O., Quach D.V., Efe M., Cantwell P.R., Heim B., Schultz B., Stach E.A., Groza J.R. and Allain J.P. 2011 Multimodal grain size distribution and high hardness in fine grained tungsten fabricated by spark plasma sintering *Mater. Sci. Eng. A* **528** 5670–7
- [31] Ma J., Zhang J., Liu W. and Shen Z. 2013 Suppressing pore-boundary separation during spark plasma sintering of tungsten *J. Nucl. Mater.* **438** 199–203
- [32] Li B., Sun Z., Hou G., Ding F., Hu P. and Yuan F. 2016 The sintering behavior of quasi-spherical tungsten nanopowders *Int. J. Refract. Met. Hard Mater.* **56** 44–50
- [33] Liu R., Xie Z.M., Fang Q.F., Zhang T., Wang X.P., Hao T., Liu C.S. and Dai Y. 2016 Nanostructured yttria dispersion-strengthened tungsten synthesized by sol-gel method *J. Alloys Compd.* **657** 73–80
- [34] Xie Z.M. et al 2016 High thermal shock resistance of the hot rolled and swaged bulk W-ZrC alloys *J. Nucl. Mater.* **469** 209–16
- [35] Zinkle S.J. and Snead L.L. 2014 Designing radiation resistance in materials for fusion energy *Annu. Rev. Mater. Res.* **44** 241–67
- [36] Beyerlein I.J., Caro A., Demkowicz M.J., Mara N.A., Misra A. and Uberuaga B.P. 2013 Radiation damage tolerant nanomaterials *Mater. Today* **16** 443–9

- [37] Kajita S., Yoshida N., Ohno N. and Tsuji Y. 2015 Growth of multifractal tungsten nanostructure by He bubble induced directional swelling *New J. Phys.* **17** 043038
- [38] de Broglie I., Beck C.E., Liu W. and Hofmann F. 2015 Temperature dependence of helium-implantation-induced lattice swelling in polycrystalline tungsten: x-ray micro-diffraction and Eigenstrain modelling *Scr. Mater.* **107** 96–9
- [39] Harrison R.W., Greaves G., Hinks J.A. and Donnelly S.E. 2017 A study of the effect of helium concentration and displacement damage on the microstructure of helium ion irradiated tungsten *J. Nucl. Mater.* **495** 492–503
- [40] Trinkaus H. 1983 Energetics and formation kinetics of helium bubbles in metals *Radiat. Eff.* **78** 189–211
- [41] Iwakiri H., Yasunaga K., Morishita K. and Yoshida N. 2000 Microstructure evolution in tungsten during low-energy helium ion irradiation *J. Nucl. Mater.* **283–7** 1134–8
- [42] Chookajorn T., Murdoch H.A. and Schuh C.A. 2012 Design of stable nanocrystalline alloys *Science* **337** 951–4
- [43] Dong Z., Liu N., Ma Z., Liu C., Guo Q. and Liu Y. 2017 Preparation of ultra-fine grain W-Y₂O₃ alloy by an improved wet chemical method and two-step spark plasma sintering *J. Alloys Compd.* **695** 2969–73
- [44] Wang Z., Yuan Y., Arshad K., Wang J., Zhou Z., Tang J. and Lu G.H. 2017 Effects of tantalum concentration on the microstructures and mechanical properties of tungsten-tantalum alloys *Fusion Eng. Des.* **125** 496–502